Date of publication xxxx 00, 0000, date of current version xxxx 00, 0000.

Digital Object Identifier XX.XXXX/ACCESS.2017.DOI

Graphene Based THz Electromagnetic Imaging System for the Analysis of Artworks

SAMUEL VER HOEYE (Member, IEEE), MIGUEL FERNÁNDEZ, CARLOS VÁZQUEZ, ANDREA I. HADARIG, RENÉ CAMBLOR, LETICIA ALONSO (Student Member, IEEE) and FERNANDO LAS-HERAS (Senior Member, IEEE)

All the authors are with the University of Oviedo, Department of Electrical Engineering, Gijón, E33203, Spain

Corresponding author: Miguel Fernández (e-mail: fernandezgmiguel@uniovi.es).

This work was supported by the European Union Seventh Framework Programme (FP/2007-2013) under project 600849, by the Spanish Agencia Estatal de Investigación (AEI) and Fondo Europeo de Desarrollo Regional (FEDER) under projects TEC2016-80815-P (AEI/FEDER, UE) and TEC2015-72110-EXP (AEI), and by the Gobierno del Principado de Asturias (PCTI/FEDER-FSE) under projects IDI/2016/000373 and IDI/2017/000083.

ABSTRACT In this work, a graphene based electromagnetic imaging system working in the 140-220 GHz frequency band for nonintrusive analysis of three-dimensional artwork is presented. A single-stage high-order frequency multiplier is used to generate the signal at the transmitter module, whereas a single-stage high-order subharmonic mixer acts as signal detector at the receiver. Both modules exploit the nonlinear response of graphene sheets excited by an incident electromagnetic wave, to generate harmonic components and mixing products of the input signals, respectively. The transmitter and the receiver modules were implemented through an additive manufacturing process. The resulting electromagnetic imaging system prototype was applied to the analysis of ceramic vessels, showing its ability to detect enclosed objects and to obtain information in cross-sectional planes. Furthermore, geometrical parameters and filling material characterization can be obtained by processing the frequency response of the scattered field.

INDEX TERMS Frequency multiplier, graphene, subharmonic mixer, submillimeter wave devices, stereolithography.

I. INTRODUCTION

THE penetration properties in nonmetallic materials and the non-harmful nature of electromagnetic radiation in submillimeter wave and low THz frequency bands makes it suitable for its use in imaging applications in fields as diverse as medicine [1]–[4], pharmaceuticals [5], security [6], non-destructive testing [7], or analysis of artwork [8], among many others. However, the cost-effective practical implementation of electronic devices in these frequency bands is still a technological challenge that conditions their development, giving rise to the well known 'THz gap'.

Signal generation in the submillimeter wave and low THz frequency bands is usually achieved through frequency multipliers based on Schottky diodes [9], [10]. Although these devices provide state-of-the-art efficiency values when the multiplication order is $N = 2$ or 3, it rapidly decreases as N increases. The most common approach to overcome this problem is based on topologies in which low order frequency multipliers, with $N = 2$ or 3, are connected in cascade [11], [12], generally requiring the use of inter-stage auxiliary devices such as amplifiers and isolators. On the other hand, signal detection is usually performed by using subharmonic mixers [13]–[16]. In this case, the required local oscillator signal, generally at a frequency close to that of the RF input signal, is generated from a low frequency signal through frequency multiplication. As in the case of the multipliers, the main disadvantages of the described approach are the necessity of several stages to reach the submillimeter wave band and the requirement of power amplifiers to drive each multiplier stage, which result in highly complex and expensive systems.

In recent years, it has been theoretically predicted that graphene exhibits a strong nonlinear response when it is illuminated with an electromagnetic wave [17], [18]. In this way, an isolated graphene layer exposed to a monochromatic strong electromagnetic field at frequency ω generates a cur-

rent J that can be expressed as:

$$J \propto \left\{ \sin(\omega t) + \frac{1}{3}\sin(3\omega t) + \frac{1}{5}\sin(5\omega t) + \cdots \right\} \quad (1)$$

From (1), the generated current is composed of an infinite set of odd-order harmonic components with and amplitude that slowly decays with the harmonic order N, and that does not depend on the magnitude of the excitation field, provided that it is greater than a certain threshold [17]. The threshold depends on the temperature and the frequency ω, and the theoretical predictions show that, at room temperature, the behavior described in (1) can be achieved at frequencies from the microwave to the low THz bands. However, in practice, the graphene will usually contain impurities and it will be deposited on a substrate, causing additional interactions. Under these conditions, it has been predicted that the nonlinear response is still observable, but the field level threshold will increase [18]. The phenomenon has been experimentally verified directly on isolated graphene samples [19], [20], in samples encapsulated in high-quality crystal substrates [21], and in simple microwave devices [24], [25]. The described behavior, combined with its predicted extremely broad bandwidth, and with the relatively low cost of graphene sheets, creates the possibility of developing a radically new and cost-effective technology capable of overcoming the current THz gap.

A wide variety of experiments have demonstrated the validity of the theoretical predictions from the microwave to the optical domains, and practical devices based on them have been reported. On the one hand, graphene based field-effect transistors (G-FET) working in the millimeter [22] and submillimeter wave [23] bands have been presented, and their application to the design of frequency multipliers and mixers in the microwave [26], [27] and submillimeter wave [28] frequency bands has also been described. However, these devices operate as second or third order multipliers, not fully exploiting the high potential of graphene. Furthermore, the performance of the G-FET is strongly conditioned by the available fabrication processes. On the other hand, the ability of graphene to generate high order harmonic components from a given excitation signal has been experimentally characterized using simpler setups, as coplanar waveguides over a graphene sheet [24], [25], or graphene films integrated in narrow gaps etched in microstrip transmission lines working as microwave frequency multipliers [29], millimeter wave mixers [30], or subharmonic mixers [31]. However, the best results to date have been obtained by integrating an structured few-layer graphene sheet into a waveguide structure to obtain submillimeter wave high-order frequency multipliers [32], [33] and subharmonic mixers [34], [35].

In this work, a graphene based electromagnetic imaging system working in the $140 - 220$ GHz frequency band is described. The system is applied to the analysis of sealed ceramic vessels in order to determine geometric parameters, such as as the wall thickness, or to detect the presence of a filling material, and to estimate its composition.

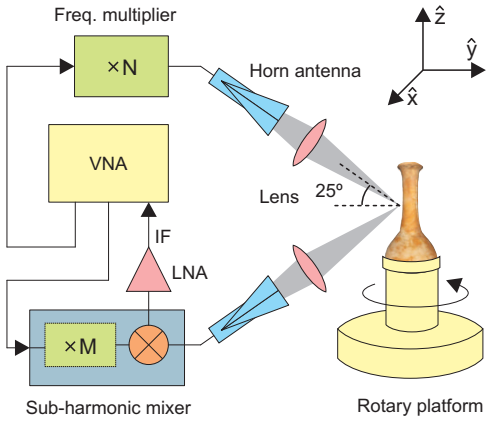

FIGURE 1. Topology of the scanner. Signal beams are parallel to the XY plane.

The paper is organized as follows. In section II, the scanner topology is presented, and the transmitter and receiver modules are described. Section III provides some implementation details and the experimental characterization of the scanner performance. Section IV is devoted to the application of the scanner to the analysis of ceramic vessels, including the detection of hidden objects, and the analysis of the filling materials.

II. SCANNER DESCRIPTION

A. TOPOLOGY

The scanner topology is similar to that proposed in [8], and it is schematized in Fig. 1. It is composed of a pair of transmitter and receiver modules mounted in a quasi-monostatic configuration, and working in the $140 - 220$ GHz frequency band, which is attached to a robotized three-axis positioning system. The object under test is placed on a rotating platform, and illuminated under a 25^o angle. The scattered signal is downconverted to an intermediate frequency $f_{IF} = 300$ MHz at the receiver module. A focusing system composed of two biconvex dielectric TPX lenses with a focal distance of 25 mm is used to improve the scanner resolution. The setup is completed with a laser-based autofocus system which enables the use of the scanner to analyze three-dimensional objects. Finally, a Vector Network Analyzer (VNA) is used to provide the input signal to the frequency multiplier, the local oscillator signal to the sub-harmonic mixer, and to measure the detected signal at intermediate frequency.

B. TRANSMITTER MODULE

A graphene based single-stage high-order frequency multiplier is used to generate the signal which illuminates the object under test, in the $140 - 220$ GHz frequency band, through frequency multiplication of a low frequency input signal in the $26 - 40$ GHz frequency band.

As represented in the 3D model shown in Fig. 2, the frequency multiplier comprises a planar stripline circuit embedded in a waveguide structure, placed parallel to the E-

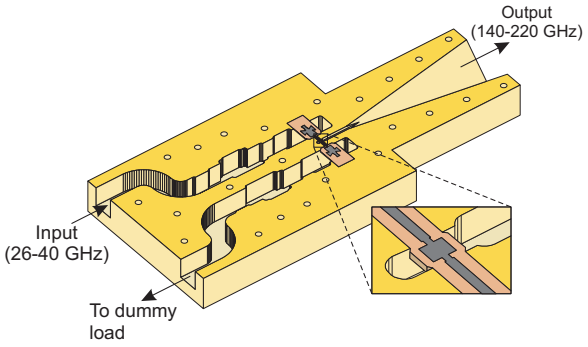

FIGURE 2. Section view of the transmitter module. The inset shows details of the planar circuit around the high-frequency transition.

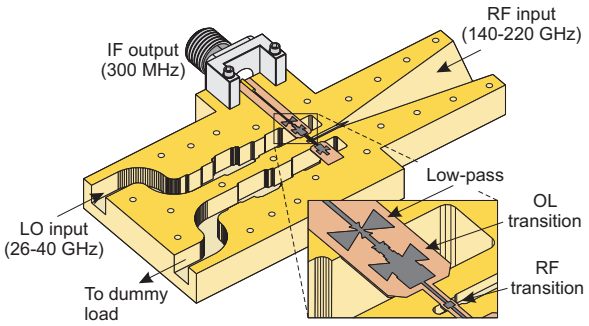

FIGURE 3. Section view of the receiver. The inset shows details of the planar circuit around the LO and RF transitions and the IF low-pass structure.

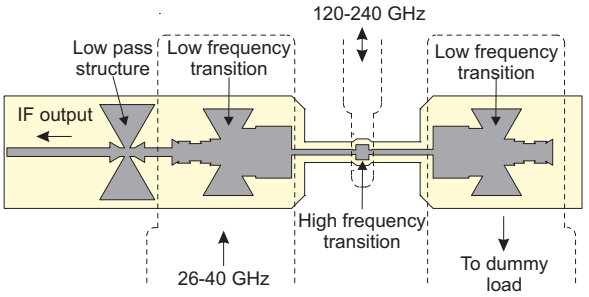

FIGURE 4. Details of the mixer planar circuit. The dark shaded area represents the sctructured graphene sheet, whereas the light shaded one represents the subtstrate. Dashed lines show the relative position of the waveguide sections. In the case of the multiplier, the planar circuit is similar, and it is obtanided by removing the low pass structure and the IF line and port.

plane [32], [33]. The stripline circuit consists of a few-layer graphene sheet transferred onto a polyimide substrate. The graphene sheet acts as circuit metallization and as frequency multiplier. It is patterned to obtain two low frequency waveguide-to-planar transitions working in the input frequency band, one high frequency transition working in the output $140 - 220$ GHz frequency band, and a line which interconnects them.

The waveguide structure includes two WR-28 waveguide sections, which are used to manage the input signal, whereas A WR-5 waveguide section is used to extract the output signal. The waveguide block also includes a channel to host the planar circuit, whose cross-section has been sized to prevent the existence of propagative modes at the operation frequencies. The main design goals are to minimize the input return losses and to maximize the coupling efficiency of the transitions. To achieve them, the shape of the transitions and that of the waveguide sections around them are optimized, and the behavior of the graphene sheet as electrical conductor is taken into account by modeling it as highly oriented pyrolytic graphite, with the adequate thickness and conductivity $\sigma = 2 \times 10^6$ S/m. Furthermore, one of the WR-28 waveguide sections is used to extract the portion of the input signal that cannot be converted to the output frequency band, avoiding in this way the use of isolators [36]. Figure 4 shows the shape of the planar circuit after the optimization process. Note that the representation corresponds to the mixer, but in the case of the multiplier, the planar circuit is similar, and it can be obtained by removing the low pass structure and the IF line and port. Finally, a diagonal horn antenna is attached to the output waveguide. In order to avoid signal losses and undesired mismatching effects at the interconnection between the two devices, the antenna is implemented together with the frequency multiplier on the same waveguide block.

One of the WR-28 waveguide sections is used to deliver the input signal, which propagates under the fundamental TE_{10} mode, to the corresponding low frequency transition, exciting the graphene. Due to the nonlinear response described in (1), a current containing odd-order harmonic components of the input signal frequency will be generated at the graphene transition. This current propagates through the planar circuit as a TEM mode, and the desired harmonic component is coupled to the output WR-5 waveguide by the high frequency transition. The portion of the input signal that is not converted is delivered to a dummy load.

The proposed topology allows the use of two different multiplication order values, $N = 5$ and $N = 7$. In the first case, the input signal frequency is contained in the range $28 - 40$ GHz and, hence, the output signal frequency varies between 140 and 200 GHz. Regarding $N = 7$, the input frequency is located between 26 and 31.4 GHz, providing an output signal in the $180 - 220$ GHz frequency range. Note that the lowest working frequency is imposed by the cut-off frequency of the waveguide sections, whereas the single-mode limit frequency conditions the maximum working frequency.

C. RECEIVER MODULE

The core of the receiver module is a graphene based high-order subharmonic mixer which downconverts the input RF signal (scattered by the object under test) with frequency f_{RF} located in the $140 - 220$ GHz frequency band, by mixing it with a high-order harmonic component of the local oscillator (LO) signal, with frequency f_{LO} in the $26 - 40$ GHz frequency band, providing the intermediate frequency (IF) output at frequency $f_{IF} = 300$ MHz.

A 3D model of the receiver module is represented in Fig. 3. Its structure is quite similar to that of the transmitter. The

main difference is found in the planar circuit, where an output port and a low-pass structure are added to extract the IF signal, and to prevent the leakage of the LO signal and its harmonic components through the IF port [34], [35].

In this case, the RF signal, coming from the receiver antenna, propagates along the WR-5 waveguide section and is coupled to the planar circuit through the high frequency transition. On the other hand, the LO signal propagates along one of the WR-28 waveguide sections and is coupled to the planar circuit at the corresponding low frequency transition. The resulting IF signal is guided to the output port, whereas the unused part of the LO signal is coupled to the other WR-28 waveguide section and delivered to a dummy load.

Due to the nonlinear response of the graphene driven by the LO signal, a current composed of harmonic components of this signal and intermodulation products between them and the RF signal is generated at the device. The frequency of the latter components can be expressed as $f_{IF} = |f_{RF} \pm M \times f_{LO}|$, with $M \in [1,\ 2,\ \cdots]$. Table 1 shows the LO frequency values required to downconvert to $f_{IF} = 300$ MHz an input signal in the $140 - 220$ GHz frequency range, for different multiplication orders M. Since the conversion efficiency decreases when increasing the multiplication order, $M = 6$ provides the best possible configuration, as it covers the whole $140 - 220$ GHz frequency band, while keeping the LO frequency approximately within the standard WR-28 waveguide operating band.

	$M = 6$	$M = 8$	$M = 10$
$f_{RF} = 140$ GHz	23.28	17.46	13.97
$f_{RF} = 180$ GHz	29.95	22.46	17.97
$f_{RF} = 220$ GHz	36.66	27.46	21.97

TABLE 1. Approximate LO frequencies, f_{LO}, in GHz, for different multiplication orders.

III. SCANNER IMPLEMENTATION AND CHARACTERIZATION

A. IMPLEMENTATION

The waveguide blocks were implemented through a stereolitography process in which a photopolymer resin is progressively cured, layer by layer, by exposing it to UV radiation. Each block is manufactured as two identical pieces resulting from dividing it along its symmetry plane, that coincides with the E-plane of the waveguide sections. Next, the surface of the resulting pieces was covered with a thin gold layer through a sputtering process.

To implement the planar circuits, a few-layer graphene film was obtained through micromechanical exfoliation of a Highly Oriented Pyrolitic Graphite (HOPG) block. Next, it was transferred onto a polyimide substrate with 50 μm thickness, dielectric constant $\varepsilon_r = 3.5$, and loss tangent $\tan\delta = 0.008$, evaluated at 300 GHz. After that, the graphene sheet was structured through a laser ablation process to obtain the desired shape.

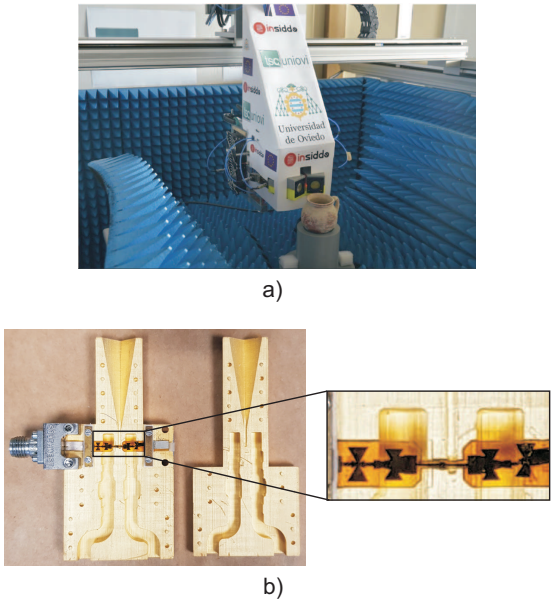

FIGURE 5. (a) Picture of the scanner prototype, mounted in an anechoic chamber while measuring a ceramic vessel. (b) Picture of the receiver module before the final assembling. The inset shows the planar circuit in detail.

A picture of the scanner prototype mounted in an anechoic chamber while measuring a ceramic vessel is shown in Fig. 5 (a), whereas the mixer prototype before assembling the two waveguide block halves is represented in Fig. 5 (b).

B. OVERALL SYSTEM PERFORMANCE

The performance of the scanner was experimentally evaluated. First, the directional characteristics of the transmitter, without lens, are depicted in Fig. 6. The measurement was performed by mounting the transmitter module on a rotary platform, and using a VNA equipped with a frequency extender module as power detector. From Fig. 6, the diagonal horn antenna provides a 10^o -3 dB beamwidth in both main planes, which would generate a circularly shaped spot with radius 5.2 mm at a 50 mm distance, under normal incidence conditions. However, since the transmitter focuses the beam using a spherical lens with 25 mm focal distance, and works with a 25^o incidence angle, the -3 dB focused spot of the overall system is elliptically shaped, with 1.53 mm major axis and 1.25 mm minor axis. These dimensions were determined in a calibration process based on obtaining an electromagnetic image of a planar metallic cross-shaped object and comparing it with the object dimensions.

Next, the dynamic range of the complete scanner was characterized, using a metallic plate as object under test. Initially, with the transmitter switched off, the noise floor of the complete receiver was measured, obtaining a -102 dBm level. Next, with the transmitter switched on, the power received at intermediate frequency, $f_{IF} = 300$ MHz, was measured. The result is represented in Fig. 7. The scanner provides a 43 dB maximum dynamic range, evaluated at 180 GHz, which is considered sufficient for the proposed appli-

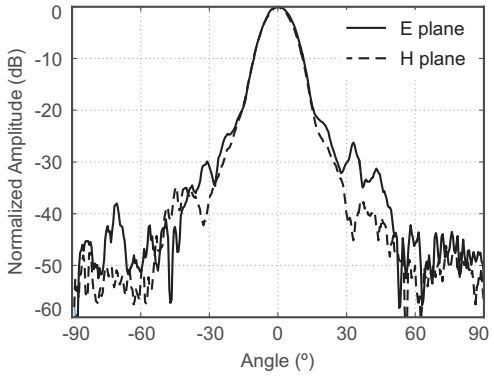

FIGURE 6. Measured directional characteristics of the transmitter module, evaluated on the two main planes of the antenna.

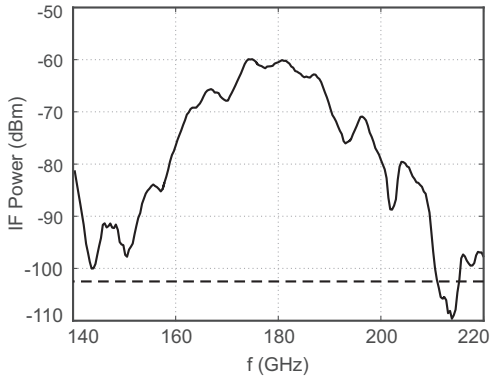

FIGURE 7. Received power level at intermediate frequency . A metallic plate is used as object under test. The dashed black trace represents the noise floor of the measurement equipment.

cation. Furthermore, the system exhibits a dynamic range greater than 23 dB over a 40 GHz bandwidth, from 160 to 200 GHz. Note that these limits depend on the overlapping responses of the frequency multiplier and the sub-harmonic mixer.

IV. RESULTS

In this section, electromagnetic images of some ancient Roman vessels are presented. The collected data are processed to detect elements inside the vessels and to characterize the wall thickness and the content of sealed vessels.

A. DETECTION OF ENCLOSED OBJECTS

In order to demonstrate the ability of the graphene based imaging system to detect objects, a metallic square helix and a ring were placed inside a ceramic vessel, as shown in Fig. 8 (a). The electromagnetic field scattered by the vessel containing the metallic objects was measured by moving the scanner head over a cylindrical surface around the vessel. The resulting normalized amplitude is represented in Fig. 9. The white dots show the position of the square helix corners, whereas the straight and rounded lines indicate the projection of the helix and the ring, respectively. The higher response is obtained at the measurement positions which correspond to

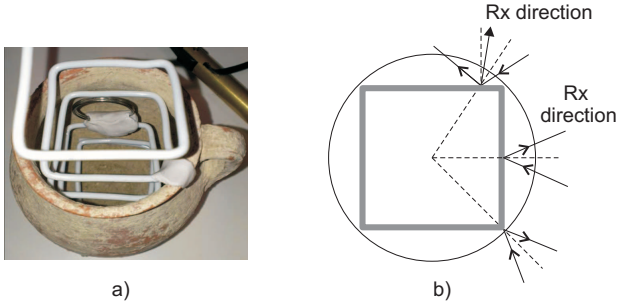

FIGURE 8. (a) Picture of a ceramic vessel used to prove the abilty to detect enclosing objects. (b) Schematic representation of the different measurement conditions. The grey thick line represents the projection of the squere helix.

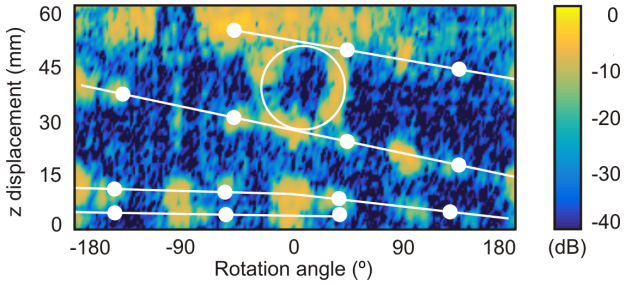

FIGURE 9. Electromagnetic image of a ceramic vessel enclosing metallic objects. White points and lines indicate the projection of the square helix corners and wire sections, respectively.

the helix corners, the middle points of the helix wire between two adjacent corners, and the ring. This is due to the fact that, at these measurement points, the scanner head is perpendicular to the metallic surfaces. Thus, most of the incident beam is scattered in the receiver direction. As opposite, the scattered signal level measured at the rest of the positions is considerably lower, since the scattered signal is out of the receiver direction, because of the circular movement of the scanner head around the vessel, which causes that at these points, the normal direction to the metallic surface is not aligned with the scanner head direction, as schematized in Fig. 8 (b). Finally, the high level signal located at the top of the picture could be due to reflections on the vessel edge. In this way, in addition to the ability to detect hidden objects, this measurement demonstrates that the dynamic range of the scanner is high enough for the proposed application.

B. ELECTROMAGNETIC IMAGES

Subsequently, electromagnetic images of the ancient Roman (A. D. 300-400) sealed ceramic vessel represented in Fig. 10 (a) were acquired. The results, obtained at 160, 180 and 200 GHz, are shown in Fig. 10 (b), (c), and (d), respectively. To obtain the images, the scanner head was vertically swept along the $\hat{z}$ direction. For each z-position, the ceramic vessel was rotated 360^o. At each measurement point, the autofocus system was used to adjust the focus point to the outer surface of the vessel. Finally, the signal measured at each z-position, as a function of the rotation angle, is normalized with respect

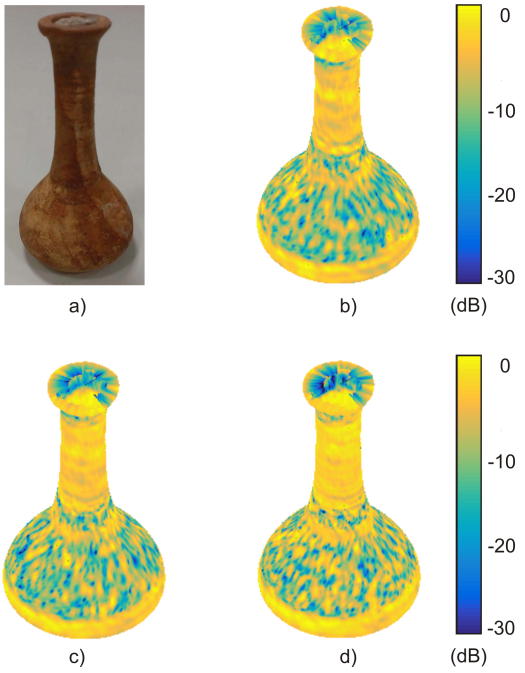

FIGURE 10. (a) Picture of the analyzed sealed vessel. Electromagnetic images of the outer surface of the vessel, evaluated at: (b) 160 GHz. (c) 180 GHz. (d) 200 GHz.

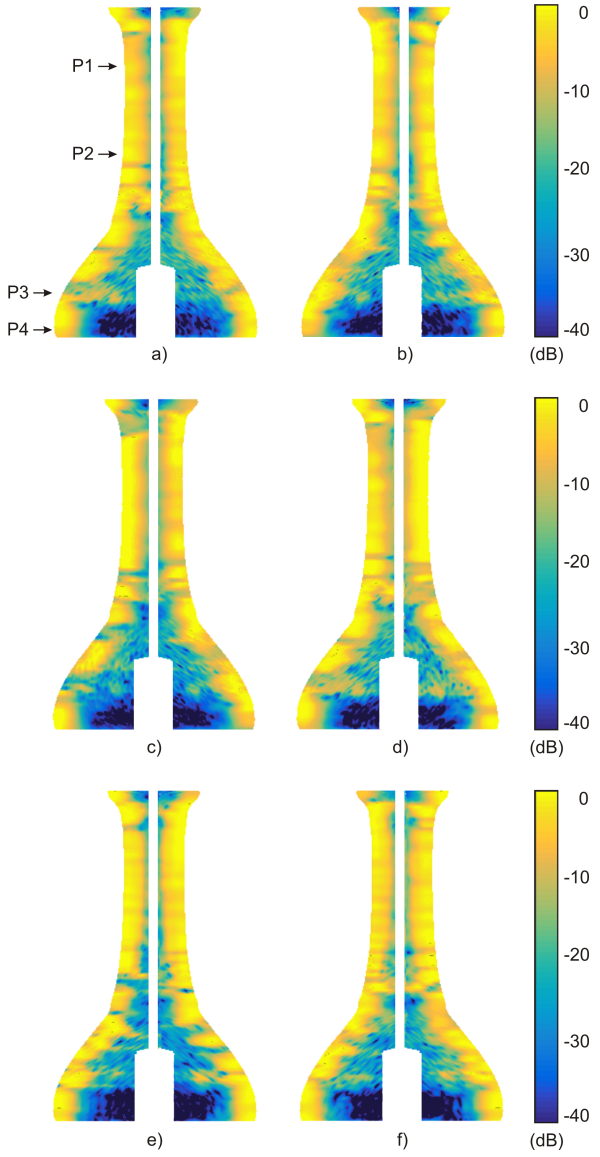

FIGURE 11. Electromagnetic images obtained on perpendicular cross-sectional planes. (a) and (b): 160 GHz, front/back views, and left/right hand side views, respectively. (c) and (d): 180 GHz, front/back views, and left/right hand side views, respectively. (e) and (f): 200 GHz, front/back views, and left/right hand side views, respectively.

to the maximum level obtained at that scanner height. Note that the absolute strength of the scattered field from the curved region of the vessel body is reduced with respect to the level measured at the neck or the bottom part, because the curved surface predominantly reflects the incident wave in directions different from that of the receiver. This effect cannot be observed in the representation of Fig. 10, since the measured field level is normalized with respect to the maximum obtained at each z-position. The reduction of the received power at these measurement points has negative impact on the scanner performance, since it limits the depth at which the scanner can provide useful information. However, the results obtained when detecting enclosed objects, or analyzing the ceramic walls and the filling material, demonstrates that the described effect does not condition the scanner viability. Furthermore, it could be overcome by mounting the scanner head on a 4-axis positioning system. In that case, the scanner could also be used to reveal vessel engravings hidden under a sediment layer.

On the other hand, to obtain information about the interior of the sealed vessel, the images shown in Fig. 11 were acquired at 160, 180 and 200 GHz. In this case, four fixed angular positions are considered, associated with the front, back, left and right side views of the vessel. To obtain the images, the focus of the scanner is moved from the outer surface towards the inside of the object under test, repeating the procedure for all considered vertical positions. Thus, information on two perpendicular cross-sectional planes which contain the longitudinal axis of the vessel is obtained. The white regions in the images correspond to zones in which no information is available due to the safety margins imposed to avoid the collision between the scanner head and the vessel.

In order to obtain the represented images, for each vertical position the measured scattered signal power is represented versus the estimated focus position, which is calculated as the horizontal displacement of the scanner head with respect a zero-position. The scanner head zero-position corresponds with the point for which the transmitted beam is focused just over the vessel surface. As long as the scanner head approaches to the vessel, the focus point penetrates inside the ceramic wall and it cannot be accurately obtained as the head displacement, due to the fact that the signal is propagating not only on air, but also in a medium with an *a priori*

unknown dielectric permittivity. In this way, this analysis provides qualitative information about the geometry of the object under test, but it has to be used in combination with the frequency response processing to obtain accurate results.

Starting with the analysis of the vessel wall from measurement data represented in Fig. 11, the variation of the reflectivity along its depth indicates that it is not uniform. This can be due to the fact that, during the ceramic curing process, the outer side is more exposed to heat than the inner surface. Another possible cause is that the internal surface is partially coated with the residue of substances that the vessel may have contained at some point. There are also certain wall zones in which a considerable reduction of the scattered field level is observed, which could be related to the presence of air bubbles.

Regarding the filling material, the uniformity of the scattered field strength when the focus is completely inside the vessel is compatible with the presence of an homogeneous material with low reflectivity. Furthermore, the homogeneity of the material increases at the vessel bottom, indicating that the material is more uniform in this region. Finally, since no strong variation in the response is observed, it is expected that the vessel does not contain any object.

C. ANALYSIS OF THE CONTENT OF SEALED VESSELS

The thickness and the relative dielectric permittivity of the ceramic wall, as well as the permittivity of the vessel filling material, can be estimated from the measured frequency response of the scattered field in the $160-200$ GHz frequency range. To do that, it is compared and matched to the theoretical frequency response of a multilayer structure, under oblique incidence, obtained using the Fresnel quasi-optical approach.

Let us consider a plane wave propagating on air which illuminates a three layer dielectric structure under a θ_0 angle, as represented in Fig. 12. The thickness and the refractive index of each layer are represented by d_i and n_i, respectively, with $i \in [0, 3]$. The medium from which the plane wave illuminates the structure is denoted as $i = 0$ layer, and the $i = 3$ layer is considered infinite. The reflection $\rho_{i,i+1}$ and the transmission $\tau_{i,i+1}$ coefficients, evaluated at the interface between two layers, when the wave propagates from layer i to layer $i + 1$, can be calculated as:

$$\rho_{i,i+1} = -\frac{\sin(\theta_i - \theta_{i+1})}{\sin(\theta_i + \theta_{i+1})} \tag{2}$$

$$\tau_{i,i+1} = \frac{2\sin(\theta_{i+1})\cos(\theta_i)}{sin(\theta_i + \theta_{i+1})} \tag{3}$$

where the propagation angle in the $i+1$ layer, θ_{i+1}, is related to that on i layer through the Snell's law:

$$\theta_{i+1} = \arcsin\left(\frac{n_i}{n_{i+1}}\sin(\theta_i)\right) \tag{4}$$

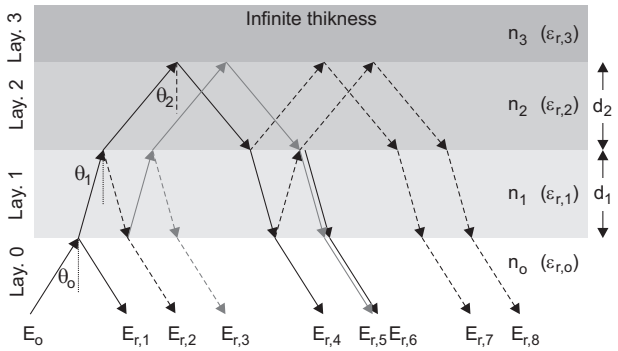

FIGURE 12. Multilayer model used to estimate the geometrical parameters and the filling of the analyzed vessels from the measured frequency response.

with $\theta_0 = 25^o$, because of the particular configuration of the scanner head. In addition, the phase variation ϕ_i due to the propagation through the i layer is given by:

$$\phi_i = \frac{2\pi f n_i}{c}\frac{d_i}{\cos(\theta_i)} \tag{5}$$

where c represents the speed of light in vacuum, and f is the working frequency. Therefore, the total scattered field E_r can be expressed as:

$$E_r = E_o \sum_k E_{r,k} \tag{6}$$

with E_o the amplitude of the incident wave, and the contributions $E_{r,k}$ indicated in Fig. 12, with $k = 1, \cdots, 8$, calculated from the reflection, transmission, and phase coefficients expressed in (2), (3), and (5), respectively. Note that contributions to the scattered field that are out of the receiver spot can be neglected in (6). Finally, to estimate the thickness d_i and the relative dielectric permittivity $\varepsilon_{r,i} = n_i^2$ of each layer, the measured frequency response is compared with (6) to obtain an error function which is minimized in a Newton gradient based optimization process, being the optimization variables d_i and $\varepsilon_{r,i}$.

For a fixed rotation angle, coincident with the front view, the scanner head is moved to four different height positions, indicated in Fig. 11 (a), two of them on the neck and the other two on the vessel body, and the focus is adjusted to be on the outer surface of the vessel. Taking into account the information about the wall obtained from the electromagnetic images shown in Fig. 11, the problem was modeled with three layers, two of them for the wall, and the innermost for the filling. The obtained results are displayed in Table 2, whereas the comparison between the measured frequency response and that of the optimized model is represented in Fig. 13. First, the thickness of the wall at the measurement points can be calculated from the obtained data. Next, the small variation of the dielectric constant of the third layer is coherent with the assumption that the filling material is relatively homogeneous. Finally, the reduction of the dielectric pertimittivity observed at the measurement point 3, could be associated to a local reduction of the material density, possibly caused by an air bubble.

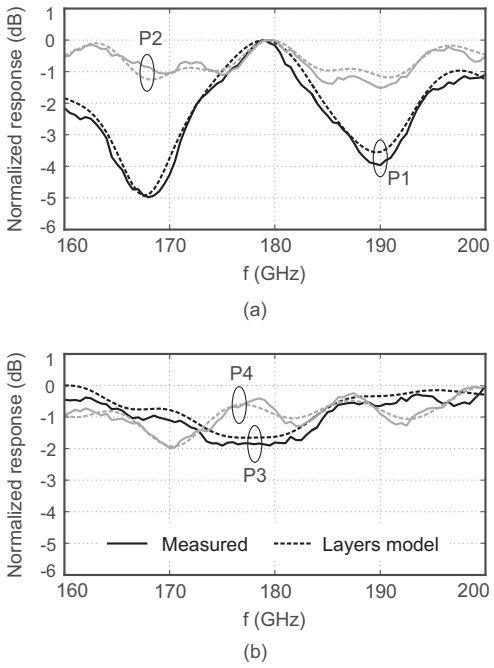

FIGURE 13. Comparison between the measured frequency response and the one adjusted from the layer model. (a) Points on the vessel neck. (b) Points on the vessel body.

Finally, it should be remarked that the opposite ceramic wall is not taken into account in the model, due to the following reasons. On the one hand, contributions to the scattered field coming from a point away from the outer surface cannot be detected, since they are out of the receiver spot. On the other hand, due to the limited available power at the transmitter and the effect of successively multiplication of low reflection coefficients, its influence on the measured frequency response is negligible.

	Layer 1		Layer 2		Layer 3
	Thick. (mm)	ε_r	Thick. (mm)	ε_r	ε_r
Point 1	1.8	2.7	3.1	2.4	3.0
Point 2	3.1	2.5	2.5	2.2	3.3
Point 3	1.0	3.2	2.5	1.9	3.0
Point 4	2.3	4.0	2.4	4.1	3.0

TABLE 2. Estimated thickness and dielectric permittivity of the layers used to model the frequency response.

V. CONCLUSION

An electromagnetic imaging system working in the low THz frequency band for the nondestructive analysis of artwork has been presented. Signal generation and detection are accomplished by exploiting the strong nonlinear behavior of few-layer graphene sheets under electromagnetic excitation. The data provided by the scanner has been processed to analyze ancient ceramic vessels, showing its ability to detect enclosed objects, to estimate geometrical parameters such as the thickness of the ceramic walls, and to provide information about the filling material in sealed vessels. Finally, the performance of the scanner demonstrates that graphene based circuitry represents a viable cost-effective alternative to traditional semiconductor based technology to develop systems and applications operating in the submillimeter wave and low THz frequency bands.

ACKNOWLEDGMENT

The authors thank the Regional Museum of History of Stara Zagora (Bulgaria), for the lending of the ceramic vessels used in the presented analysis.

REFERENCES

[1] G. G. Hernandez-Cardoso, S. C. Rojas-Landeros, M. Alfaro-Gomez, A. I. Hernandez-Serrano, I. Salas-Gutierrez, E. Lemus-Bedolla, A. R. Castillo-Guzman, H. L. Lopez-Lemus, E. Castro-Camus, "Terahertz imaging for early screening of diabetic foot syndrome: A proof of concept," *Sci. Rep.*, vol. 7, Feb. 2017.

[2] F. Dornuf, P. Martín-Mateos, B. Duarte, B. Hils, O. E. Bonilla-Manrique, F. Larcher, P. Acedo, V. Krozer, "Classification of skin phenotypes caused by diabetes mellitus using complex scattering parameters in the millimeter-wave frequency range," *Sci. Rep.* vol. 7, Jul. 2017.

[3] P. Martín-Mateos, F. Dornuf, B. Duarte, B. Hils, A. Moreno-Oyervides, O. E. Bonilla-Manrique, F. Larcher, V. Krozer, P. Acedo, "In-vivo, non-invasive detection of hyperglycemic states in animal models using mm-wave spectroscopy," *Sci. Rep.* vol. 6, Sep. 2016.

[4] Taylor, Z. D. et. al. "THz medical imaging: in vivo hydration sensing," *IEEE Trans. THz Sci. Technol.* vol. 1, no. 1, pp. 201-219, Aug. 2011.

[5] R. K. May, M. J. Evans, S. Zhong, C. Byers, L. F. Gladden, Y. Shen, J. A. Zeitles, "Terahertz pulsed imaging of surface variations on pharmaceutical tablets," *in Proc. 35th Ing. Infrared Millim. THz Waves Conf.*, Rome, 2010.

[6] A. Luukanen, R. Appleby, M. Kemp, N. Salmon, "Millimeter-wave and terahertz imaging in security applications," in *Terahertz Spectroscopy and Imaging. Springer Series in Optical Sciences*, vol. 171, Berlin, Springer, pp. 491-520, 2012.

[7] Kemp, I., Peterson, M., Benton, C. & Petkie, D. T. Sub-mm wave imaging techniques for non-destructive aerospace materials evaluation. in Proc. IEEE Aerosp. Electron. Conf. (2009).

[8] C. Vázquez *et. al.* "Millimetre wave imaging system for the detection of hidden elements in artwork," *in Proc. Int. Conf. Electr. Advanced Appl.*, Palm Beach, 2014.

[9] E. Schlecht *et. al.* "200, 400 and 800 GHz Schottky diode substrateless multipliers: Design and Results," *in Proc. IEEE MTT-S Int. Microw. Symp. Dig.*, Phoenix AZ, 2001.

[10] C. Lee *et. al.* "A wafer-level diamond bonding process to improve power handling capability of submillimeter-wave Schottky diode frequency multipliers," *in Proc. IEEE MTT-S Int. Microw. Symp. Dig.*, Boston MA, 2009.

[11] R. J. Dengler, F. Maiwald, P. H. Siegel, "A compact 600 GHz electronically tunable vector measurement system for submillimeter wave imaging," *in Proc. IEEE MTT-S Int. Microw. Symp. Dig.*, San Francisco CA, 2006.

[12] T. W. Crowe, J. Hesler, S. Retzloff, C. Pouzou, G. Schoenthal, "Solid state LO sources for greater than 2 THz," *in Proc. 22nd Int. Symp. Space THz Technol.*, Tucson AZ, 2011.

[13] B. Thomas, A. Maestrini, G. Beaudin, "A low-noise fixed-tuned 300-360 GHz sub-harmonic mixer using planar Schottky diodes," *IEEE Microw. Wireless Compon. Lett.* vol. 15, no. 12, pp. 865-867, Dec. 2005.

[14] E. Schlecht, "A unique 520-590 GHz biased subharmonically-pumped Schottky mixer," *IEEE Microw. Wireless Compon. Lett.* vol. 17, no. 12, pp. 879-881, Dec. 2007.

[15] B. Thomas, S. Rea, B. Moyna, B. Alderman, D. Matheson, "A 320-360 GHz subharmonically pumped image rejection mixer using planar Schottky diodes," *IEEE Microw. Wireless Compon. Lett.* vol. 19, no. 2, pp. 101-103, Feb. 2009.

[16] A. Lisauskas, S. Boppel, M. Mundt, V. Krozer, H. G. Roskos, "Subharmonic mixing with fiel-effect transistors: Theory and experiment at 639 GHz high above f_T," *IEEE Sensors J.* vol. 13, no. 1, pp. 124-132, Jan. 2013.

[17] S. A. Mikhailov, "Non-linear electromagnetic response of graphene," *Europhys. Lett.*, vol. 79, no. 2, Jun. 2007.

[18] S. A. Mikhailov, K. Ziegler, "Non-linear electromagnetic response of graphene: Frequency multiplication and the self-consistent ELD effect," *J. Phys. Condens. Matter*, vol. 20, 2008.

[19] K. I. Bolotin, K. J. Sikes, Z. Jiang, M. Klima, G. Fudenberg, J. Hone, P. Kim, H. L. Stormer, "Ultrahigh electron mobility in suspended graphene," *Solid State Commun.*, vol. 146, no. 9-10, pp. 351-355, Jun. 2008.

[20] E. Hendry, P. J. Hale, J. Moger, A. K. Savchenko, S. A. Mikhailov, "Coherent nonlinear optical response of graphene," *Phys. Rev. Lett.* vol. 105, Aug. 2010.

[21] A. S. Mayorov, R. V. Gorbachev, S. V. Morozov, L. Britnell, R. Jalil, L. A. Ponomarenko, P. Blake, K. S. Novoselov, K. Watanabe, T. Taniguchi, A. K. Geim, "Micrometer-scale ballistic transport in encapsulated graphene at room temperature," *Nano Lett.* vol. 11, no. 6, pp. 2396-2399, May 2011.

[22] H. Lyu, Q. Lu, J. Liu, X. Wu, J. Zhang, J. Li, J. Niu, Z. Yu, H. Wu, H. Qian, "Deep-submicron graphene field-effect transistors with state-of-art f_{max}," *Sci. Rep.* vol. 6, Oct. 2016.

[23] Z. H. Feng, C. Yu, J. Li, Q. B. Liu, Z. Z. He, X. B. Song, J. J. Wang, S. J. Cai, "An ultra clean self-aligned process for high maximum oscillation frequency graphene transistors," *Carbon*, vol. 75, pp. 249-254, Aug. 2014.

[24] M. Dragoman, D. Neculoiu, G. Deligeorgis, G. Konstantinidis, D. Dragoman, A. Cisnaru, A. A. Muller, R. Plana, "Millimeter-wave generation via frequency multiplication in graphene," *Appl. Phys. Lett.* vol 97, Aug. 2010.

[25] M. Dragoman, A. Cismaru, A. Dinescu, D. Dragoman, G. Stavrinidis, G. Konstantinidis, "Enhancement of higher harmonics in graphene-based coupled coplanar line microwave multipliers," *J. Appl. Phys.* vol. 114, 2013.

[26] M. E. Ramón, *et. al.* "Three-gigahertz graphene frequency doubler on quartz operating beyond the transit frequency," *IEEE Trans. Nanotechnol.* vol. 11, no. 5, pp. 877-883, Sep. 2012.

[27] O. Habibpour, S. Cherednichenko, J. Vukusic, K. Yhland, J. Stake, "A subharmonic graphene fet mixer," *IEEE Electron Device Lett.* vol. 33, no. 1, pp. 71-73, Jan. 2012.

[28] O. Habibpour, J. Vukusic, J. Stake, "A 30-GHz integrated sub-harmonic mixer based on a multichannel graphene FET," *IEEE Trans. Microw. Theory Techn.* vol. 61, no. 2, pp. 841-847, Feb. 2013.

[29] R. Camblor, S. Ver Hoeye, G. Hotopan, C. Vázquez, M. Fernández, F. Las Heras, "Microwave frequency tripler based on a microstrip gap with graphene," *J. Electromagn. Waves Appl.*, vol. 25, no. 14-15, pp. 1921-1929, 2011.

[30] G. R. Hotopan, S. Ver Hoeye, C. Vazquez-Antuna, R. Camblor-Diaz, M. Fernandez-Garcia, F. Las Heras-Andres, "Millimeter wave submicrostrip mixer implementation using graphene film coating," *Prog. Electromagn. Res.* vol. 118, pp. 57-69, 2011.

[31] G. R. Hotopan, S. Ver-Hoeye, C. Vazquez-Antuna, A. Hadarig, R. Camblor-Diaz, M. Fernandez-Garcia, F. Las Heras Andres, "Millimeter wave subharmonic mixer implementation using graphene film coating," *Prog. Electromagn. Res.*, vol. 140, pp. 781-794, 2013.

[32] A. I. Hadarig, C. Vázquez, M. Fernández, S. Ver Hoeye, G. R. Hotopan, R. Camblor, F. Las Heras, "Experimental analysis of the high-order harmonic components generation in few-layer graphene," *Appl. Phys. A*, vol. 118, no. 1, pp. 83-89, Jan. 2015.

[33] C. Vázquez, A. Hadarig, S. Ver Hoeye, R. Camblor, M. Fernández, G. Hotopan, L. Alonso, F. Las Heras, "Millimetre wave transmitter based on few-layer graphene frequency multiplier," *in Proc. 45th Eur. Microw. Conf.*, Paris, 2015.

[34] C. Vázquez, *et. al.* "High-order subharmonic millimeter-wave mixer based on few-layer graphene," *IEEE Trans. Microw. Theory Techn.* vol. 63, no. 4, pp. 1361-1369, Feb. 2015.

[35] C. Vázquez, A. Hadarig, S. Ver Hoeye, R. Camblor, M. Fernández, G. Hotopan, L. Alonso, F. Las Heras, "Millimetre wave receiver based on a few-layer graphene WR-5 band subharmonic mixer," *in Proc. Global Symp. Millim. Waves*, Montreal QC, 2015.

[36] A. Maestrini, *et. al.* "Local oscillator chain for 1.55 to 1.75 THz with 100-μW peak power," *IEEE Microw. Wireless Compon. Lett.* vol. 15, no. 12, pp. 871-873, Dec. 2005.

SAMUEL VER HOEYE (M'05) received the M.Sc. degree in electronics engineering from the University of Gent, Gent, Belgium, in 1999, and the Ph.D. degree from the University of Cantabria, Santander, Spain, in 2002.

He is currently Associate Professor with the Department of Electrical and Electronic Engineering at the University of Oviedo, Gijon, Spain. His main research is focused on the design and analysis of microwave, millimeter wave and THz circuits and systems. Among these are the multi-functional oscillator based circuits and antennas, frequency scanning antennas, graphene based frequency multipliers and mixers, imaging systems, and textile integrated high frequency components.

MIGUEL FERNÁNDEZ received the M.Sc. degree in telecommunication engineering, the M.Sc. degree in information technology and mobile communications, and the Ph.D. degree from the University of Oviedo, Gijón, Spain, in 2006, 2010 and 2010, respectively.

From 2006 to 2008, he was a Research Fellow, and since September 2008, he has been an Associate Professor, both with the Signal Theory and Communications Group, University of Oviedo. His main research effort is focused on nonlinear analysis and optimization techniques for the design of oscillator-based circuits, active antennas and frequency multipliers and mixers at the microwave, millimeter/submillimeter-wave, and terahertz frequency bands.

CARLOS VÁZQUEZ received the M.Sc. degree in telecommunication engineering, M. Sc. degree in information technology and mobile communications, and Ph.D. degree from the University of Oviedo, Gijón, Spain, in 2007, 2008, and 2013, respectively.

From 2007 to 2012, he was a Graduate Research Assistant, and since 2012, a Research Fellow with the Signal Theory and Communications Group, University of Oviedo. His research efforts mainly focus on nonlinear analysis and optimization techniques for the design of multifunctional oscillator-based circuits, active antennas and passive components, such as frequency multipliers and harmonic mixers, at microwave, millimeter/submillimeter-wave, and terahertz frequencies.

ANDREEA I. HADARIG received the B. Sc. degree in telecommunication engineering from the Technical University of Cluj Napoca, Romania, in 2012, the M. Sc. degree in information technology and mobile communications from the University of Oviedo, Spain, in 2013, and the Ph. D. degree from the University of Oviedo, in 2017.

Since 2012, she has been a Research Assistant with the Signal Theory and Communications Group, University of Oviedo. Her main research effort is focused on the design, optimization, and analysis of passive devices using waveguides and microstrip technology operating in the millimeter/submillimeter wave and THz frequency bands.

RENÉ CAMBLOR received the M. Sc. degree in telecommunication engineering, the M. Sc. degree in electromagnetic engineering, and the Ph.D. degree from the University of Oviedo, Gijón, Spain in 2006, 2010 and 2015, respectively, and the LL. M. degree from the UNED, Madrid, Spain, in 2013.

Since 2009, he has been a Research Engineer with the Signal Theory and Communications Group, at the University of Oviedo. His current research interests are submillimeter-wave antennas and terahertz systems.

LETICIA ALONSO received the M. Sc. degree (2014) in telecommunication engineering from the University of Oviedo, Gijón, Spain, the M. Sc. degree (2018) in Systems and Control Engineering from the National University of Distance Learning (UNED) and the Universidad Complutense de Madrid, Spain, and the Ph. D. degree (2018) from the University of Oviedo.

Since 2014, she has been working as a researcher in the Signal Theory and Communications Group, University of Oviedo. She was a Visiting Scholar at the George Green Institute for Electromagnetics Research at the University of Nottingham (UK) in 2017. Her main research effort is focused on the design, simulation and manufacturing techniques to develop microwave and millimeter wave passive circuits and antennas fully integrated in textile technology.

FERNANDO LAS-HERAS M.s. degree (1987) and Ph.D. degree (1990) in Telecommunication Engineering from the Tech University of Madrid (UPM). National Graduate Research fellow (1988-1990), Associate Professor (1991-2000) at the Dept. of Signal, Systems and Radiocom of UPM and Full Professor at the University of Oviedo (since 2003). Head of research group Signal Theory and Comm (TSC-UNIOVI) (2001-) at the Dept. of Electrical Engineering of the University of Oviedo. Vice-dean for Telecommunication Eng at the Tech School of Engineering at Gijón (2004-2008). Visiting Researcher at Syracuse University, New York, Visiting Lecturer at the National University of Engineering, Lima, and ESIGELEC, France. He held the Telefónica Chair (on 'RF Technologies', 'ICTs applied to environment and climate change' and 'ICTs and Smartcities') (2005-2015). Member of the board of directors of IEEE Spain section (2012-2015), member of the board IEEE Microwaves & Antennas Propagation Chapter (AP03/MTT17) for 2016-2018 and member of the Science, Technology and Innovation Council of Asturias, Spain (2010). He has authored over 450 technical journal and conference papers in the areas of electromagnetic radiation, propagation and scattering theory and applications as well as inverse problems.